

# Revealing the Impact of Particle Size Distribution on Ageing of Lithium-Ion Batteries with Frequency Response Analysis

Hoon Seng Chan,<sup>[a]</sup> Lars Bläubaum,<sup>[a]</sup> Dandapani Vijayshankar,<sup>[b]</sup> Fridolin Röder,<sup>[c]</sup> Christine Nowak,<sup>[d, e]</sup> André Weber,<sup>[a]</sup> Arno Kwade,<sup>[d, e]</sup> and Ulrike Krewer<sup>\*[a]</sup>

In-depth analyses, including discharge behaviour, electrochemical impedance analysis, and for the first time, nonlinear frequency response analysis, are conducted on the ageing of negative electrodes with varying particle size distribution. The electrode-resolved analysis is used to distinguish the kinetic and transport losses at the respective electrodes. For fine to medium-sized particles at the negative electrode, ageing impacts are found more on the positive electrode: the impedance and nonlinear responses increase, suggesting that the charge transfer process at the positive electrode is

worsened. Meanwhile, for coarse and broad negative particles, the impedance and nonlinear responses at negative electrodes decrease due to improved kinetics from micro-cracking. The second harmonic reveals a change in the nature of the charge transfer during ageing: the charge transfer process at the positive electrode becomes asymmetric for fine and medium-sized negative particles. Vice versa, the charge transfer process at the negative electrode becomes symmetric for coarse and broad negative particles.

## Introduction

Lithium-ion batteries have become a rapidly growing technology as the worldwide demand for cleaner and sustainable energy supply increases. Therefore, they are attractive for powering vehicles and energy storage in the electric grid. Present challenges comprise ageing mitigation during long-term operation, fast charging, and safety issues.

Depending on the operation requirements, the characteristics of lithium-ion batteries are developed and adapted. For example, high-power batteries are designed specifically with thinner electrodes, lower coating mass, smaller active particles, and a thicker separator, as compared to high-energy batteries.<sup>[1]</sup> These features allow high-power batteries to store or release a large amount of energy in a short amount of time. This leads to reduced safety risk due to lithium plating and, in the worst case, short-circuit and thermal runaway. Therefore, it is essential to examine the impact of the physical properties of the electrodes on battery performance.

One of the important physical properties of electrodes is the particle size distribution (PSD) of the active material. Studies on the impact of the active material particle size and its distribution have been conducted on different materials of positive electrodes in lithium-ion batteries, for example, LiMnO<sub>4</sub>,<sup>[2-4]</sup> LiCoO<sub>2</sub>,<sup>[5-7]</sup> LiFePO<sub>4</sub>,<sup>[8]</sup> LiNiMnO<sub>4</sub>,<sup>[9]</sup> LiNiMnCoO<sub>2</sub>,<sup>[10,11]</sup> LiNiCoAlO<sub>2</sub>.<sup>[12]</sup> Experimental and simulation results agree that fine particles at positive electrodes are beneficial for the electrochemical performance in lithium-ion batteries. Due to their higher specific surface area and shorter diffusion pathway compared to large particles, better utilization of the active material<sup>[2,3]</sup> and higher C-rate capability<sup>[5,9]</sup> can be attained. Nevertheless, fine particles have lower coulombic efficiency (CE) and poorer cycling stability as they favour surface-related side reactions due to larger specific surface area.<sup>[6,9]</sup> Furthermore, broad PSD results in a non-uniformity of local current density on the particle surface,<sup>[4,13]</sup> which causes a greater concentration gradient across the electrode thickness and larger mechanical stress in the batteries.<sup>[2]</sup> This leads to higher losses and thus deteriorates the battery's performance.

As for negative electrode, the studied materials includes graphite,<sup>[14-16]</sup> silicon,<sup>[17-19]</sup> carbon coke,<sup>[20,21]</sup> TiO<sub>2</sub>,<sup>[22,23]</sup> and red

[a] H. Seng Chan, L. Bläubaum, Dr.-Ing. A. Weber, Prof. Dr.-Ing. U. Krewer  
Institute for Applied Materials – Electrochemical Technologies  
Karlsruhe Institute of Technology  
Adenauerring 20b, 76131 Karlsruhe (Germany)  
E-mail: ulrike.krewer@kit.edu

[b] Prof. Dr.-Ing. D. Vijayshankar  
Department of Metallurgical Engineering and Materials Science  
Indian Institute of Technology Bombay  
Mumbai 400076 (India)

[c] Prof. Dr.-Ing. F. Röder  
Faculty of Engineering Science – Battery Management Methods  
University of Bayreuth  
95440 Bayreuth (Germany)

[d] C. Nowak, Prof. Dr.-Ing. A. Kwade  
Institute for Particle Technology  
TU Braunschweig  
Volkmaroder Str. 5, 38106 Braunschweig (Germany)

[e] C. Nowak, Prof. Dr.-Ing. A. Kwade  
Battery LabFactory Braunschweig  
TU Braunschweig  
Langer Kamp 8, 38106 Braunschweig (Germany)

Supporting information for this article is available on the WWW under  
<https://doi.org/10.1002/batt.202300203>

© 2023 The Authors. *Batteries & Supercaps* published by Wiley-VCH GmbH.  
This is an open access article under the terms of the Creative Commons Attribution License, which permits use, distribution and reproduction in any medium, provided the original work is properly cited.

phosphorus-graphite.<sup>[24]</sup> Like positive electrodes, the above-mentioned works agreed that fine particles offer better C-rate capability and electrochemical performance. However, some works, depending on the materials, for example, graphite<sup>[14,15]</sup> and coke,<sup>[20]</sup> revealed that fine particles favour surface-related side reactions, such as the growth of a solid-electrolyte interphase (SEI), due to larger specific surface area, which results in a poorer initial CE and cycling stability than positive electrode.<sup>[25]</sup> Nonetheless, silicon<sup>[18,19]</sup> and TiO<sub>2</sub><sup>[23]</sup> with fine particles still show profound cycling stability. Yet, the same group of carbonaceous negative electrode material but with different forms or structures has led to a different ageing pattern.<sup>[26]</sup>

In our previous study,<sup>[14]</sup> we investigated mesocarbon microbeads graphite particles (MCMB), particles of spherical form, with four different PSDs. It is shown that fine to middle-sized PSD led to capacity loss mainly due to surface-related side reactions such as SEI formation. Interestingly, lithium plating was observed on the particle surface of coarse and broad PSD right after formation due to the slow charge transfer and diffusion kinetics. However, for cells with these PSD, a notable decrease in overall kinetic and transport losses during cycling was observed. There, micro-cracking could have taken place because a small specific surface area leads to a high local current density on coarse graphite particles, as also observed in.<sup>[27–29]</sup> Also, cells with broad and coarse PSD showed significant degradation behaviour as they contain the ageing effect of both fine and broad particles.

Likewise, Zavalis et al.<sup>[30]</sup> studied the ageing behaviour of MCMB graphite particles under a dynamic cycling profile with high C-rates up to 5 C. The investigated MCMB graphite particles have similar PSD and porosity as the coarse fraction that we implemented in our previous study<sup>[14]</sup> but smaller electrode mass loading and lower height. Contrary to our results, Zavalis et al. reported that no lithium plating was observed, but cracks were seen on the particle surface. Further, the authors suggested accelerated growth of SEI film on the cracked surface that leads to substantial kinetic and transport losses.

Meantime, Buqa et al.<sup>[15]</sup> and Zhang et al.<sup>[31]</sup> analyzed the effect of PSD on synthetic flake graphite (SFG). As compared to MCMB, SFG attains a flakey, flat, plate-like form. With SFG, the authors didn't observe any lithium plating occurrence at coarse graphite particles even up to 20 C, although the studied particle size is larger, and the electrode mass loading, as well as the porosity, are in about the same range as reported in our previous work.<sup>[14]</sup> The authors concluded that coarse particles also show better capacity retention in long-term cycling.

In most of the above-mentioned studies, C-rate tests and galvanostatic cycling were used to characterize the electrochemical performances of lithium-ion batteries. The former analyses the combined kinetic behaviour of the batteries concerning different current loads, while the latter investigates the performance stability under continuous constant current charge and discharge. However, both methods could not characterize the internal state of the batteries distinguishably, whereby the deconvolution of the losses into charge transfer,

mass transport, ohmic and contact losses can only be determined via a specially constructed system<sup>[32]</sup> or sophisticated characterization methods.

To mitigate these shortcomings, frequency response analyses were used in our previous<sup>[33–35]</sup> and this study. For example, electrochemical impedance spectroscopy (EIS) is performed to identify the individual losses at a defined state-of-charge (SOC). While EIS is limited to linear interpretation of the system behaviour, nonlinear characterization via nonlinear frequency response analysis (NFRA)<sup>[36–38]</sup> extends the analysis to the nonlinear nature of the involved reactions in batteries. Therefore, NFRA is used in this study. Several publications on NFRA indicate its ability to extract additional information compared to EIS, for example, charge transfer symmetry,<sup>[39,40]</sup> lithium plating detection,<sup>[41]</sup> prediction of capacity fade, and identification of ageing causes.<sup>[42,43]</sup>

In this work, we aim to build a deeper understanding of the ageing behaviour of cells with negative electrodes with different PSD. As mentioned before, apart from EIS, we additionally consider NFRA to include ageing-induced changes in the nonlinear behaviour resulting from different PSD. Contrary to our previous study, both EIS and NFRA will be carried out in an electrode-resolved manner to separate the contributions from negative and positive electrodes, which will give new and deeper insights into the performance degradation with different PSD.

## Results and Discussion

In the following, the effect of PSD on the performance of formatted cells (pristine state), including their dynamic behaviour, is analyzed. This is followed by an ageing study, which reveals the change in the performance and frequency response spectra that can be related to ageing processes.

### Pristine state

The states of the battery cells with different PSD were characterized right after the formation step. Complementary to EIS, the distribution of relaxation times (DRT) technique was implemented for a clearer separation of processes with different time constants.<sup>[44]</sup> These processes were then analyzed deeper with NFRA to observe the nonlinear behaviour of these processes.

Figure 1(a) shows the full cell DRT spectrum at SOC 50% directly after formation for cells with different PSD at negative electrode: F1 (fine), F2 (middle), F3 (coarse), and SM (broad). Figure 1(b) displays the respective Nyquist diagram of the EIS. From the full cell DRT spectrum, two to three main peaks can be identified in the trusted region of the spectra: one peak between 1 Hz to 10 Hz, another from 10 Hz to 10<sup>2</sup> Hz and the third one above 10<sup>2</sup> Hz. Overall, characteristic frequencies and peak height change with PSD. The peak height decreases with decreasing particle size. Electrode-resolved analysis, as shown in Figure 1(c and d) allows assigning these peaks and dynamic

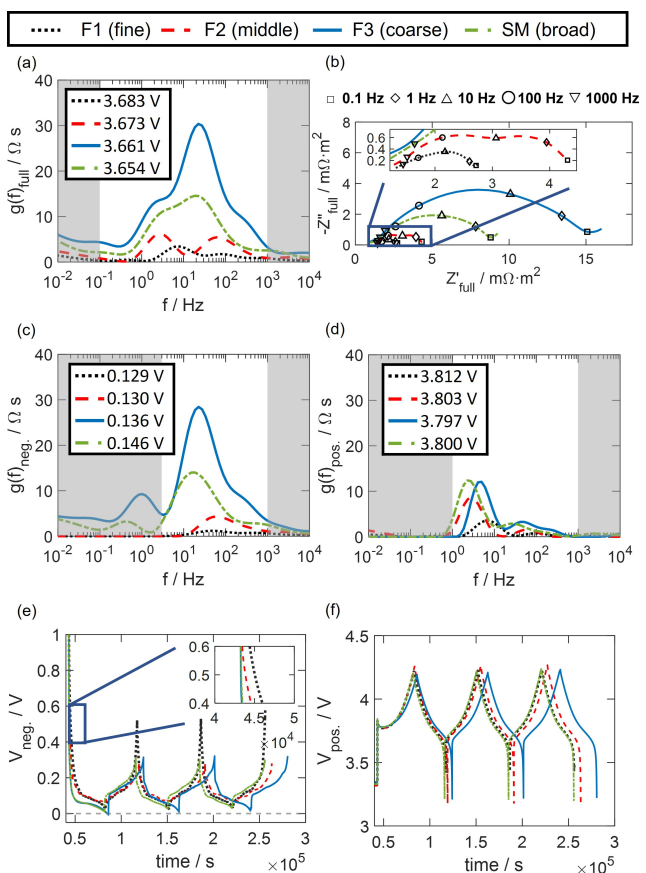


**Figure 1.** Impedance and DRT spectra after formation at SOC 50 % for cells with F1 (fine), F2 (middle), F3 (coarse) and SM (broad) PSD at the negative electrode recorded at 25 °C: full cell a) DRT and b) EIS spectra, electrode-resolved DRT spectra at c) negative and d) positive electrodes. The shaded area indicates less reliable DRT data. The given voltages indicate the open circuit potentials that correspond to the SOC 50 % adjustment. Half-cell potentials at the e) negative and f) positive electrodes during formation.

phenomena to negative and positive electrodes. Here, one can identify that the peak in the low-frequency region (1 Hz to 10 Hz) is attributed to the positive electrode while the two higher ones (10 Hz to 10<sup>2</sup> Hz and above 10<sup>2</sup> Hz) are mostly from the negative electrode with minute contribution from the positive electrode. The DRT spectra for the negative electrodes in Figure 1(c) show three peaks in total. The first peak at a lower frequency ranging from 10<sup>-1</sup> Hz to 1 Hz arises from a measurement artefact (for further details please see Supporting Information S.2) and will not be considered in further analysis. The assignment of the peaks in the DRT to physicochemical processes in the cell is based on prior studies.<sup>[36,45]</sup> The second peak at about 10 Hz to 10<sup>2</sup> Hz is related to the charge transfer process, i.e., de-/intercalation at the negative electrode/electrolyte interphase and the third peak above 10<sup>2</sup> Hz is attributed to the ionic transport across the SEI layer. Comparing the DRT spectra of negative electrodes for the various PSD, it can be generally observed that the peak height that can be correlated to the charge transfer kinetics increase and the corresponding characteristic frequency decreases with increasing particle size. Finer particles have a larger specific surface area, which favours

a fast charge transfer process. Thus, a smaller impedance or smaller DRT peak is observed for finer particles.

The DRT spectrum at the positive electrode in Figure 1(d) shows two peaks. The peak at around 1 Hz to 10 Hz is attributed to the charge transfer process, i.e., de-/intercalation at the positive electrode/electrolyte interphase and the smaller peaks at frequencies >10 Hz are attributed to ionic transport in the pores of the positive electrode along the electrode thickness.<sup>[46]</sup> All the impedance spectra and DRTs at the positive electrode were initially expected to be identical for all cells since a similar positive electrode is used in all cells. Yet, from Figure 1(d), it is obvious that this is not the case. Considering the main peak, the height and relaxation frequencies differ. Especially in the case of a fine powder, a significant difference is observed. Only a small part of these differences is related to the reproducibility in cell manufacturing, as shown in Supporting Information S.3. The major impact is the difference in the electrode balancing of different PSDs during formation. Fine particles (F1) with a larger mass-specific surface area exhibit smaller charge transfer kinetic losses at the negative electrode and simultaneously favour surface-related side reactions such as SEI formation, leading to loss of active lithium and affecting electrode balancing overall as shown in Figure 1(e and f). This results in the difference in lithium concentration distribution or lithiation degree in the positive electrode as indicated by the half-cell potential in Figure (d), which can be therefore related to the change in the EIS of the positive electrode for F1 (fine).

The attribution of peaks to certain processes is substantiated by NFR analysis: charge transfer processes should show significant nonlinearities, whereas transport across the SEI and ionic transport should show negligible nonlinearities.<sup>[36,38]</sup> In Figure 2, the full cell NFR spectrum of the cell with F1 (fine) shows nonlinear behaviour only below 10 Hz. By comparing the electrode-resolved NFR spectra, the nonlinear signal from the

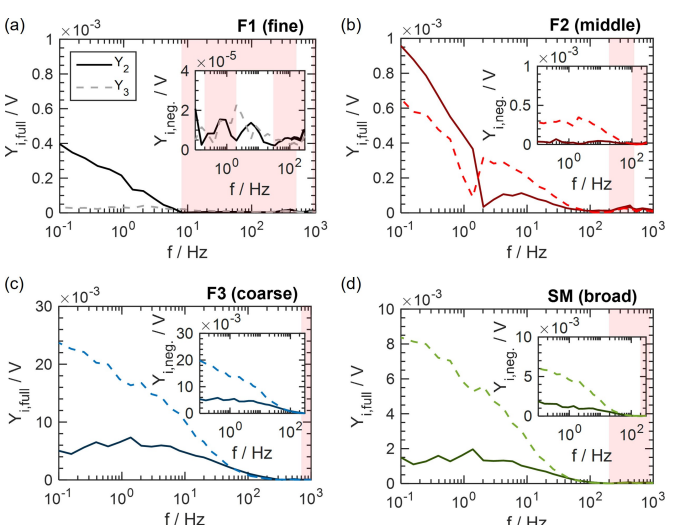


**Figure 2.** Full cell NFR spectra for cells with fractions a) F1 (fine), b) F2 (middle), c) F3 (coarse) and d) SM (broad) recorded after formation at 25 °C and SOC 50 %. Y<sub>2</sub> (solid lines) vs. Y<sub>3</sub> (dashed lines). The insets show the corresponding NFR spectra of the negative electrode. The red regions indicate unreliable regions for NFRA.

negative electrode is about two orders of magnitude smaller than the full cell, as shown in the inset of Figure 2(a). Thus, the nonlinear signals in full cell stem mainly from the positive electrode, and a correct attribution of this area to the charge transfer process at the positive electrode is confirmed. In contrast to F1 (fine), the full cell NFR spectra of cells with fractions F2 (middle), F3 (coarse) and SM (broad) feature nonlinear responses starting already from higher frequencies around  $10^2$  Hz, which is characteristic to charge transfer processes at the negative electrode. For F3 (coarse) and SM (broad), the nonlinear response at the negative electrode is similarly large as the full cell response. This confirms the attribution of the nonlinear responses within the designated frequency range to the de-/intercalation at the negative electrode. For F2 (middle), at a higher frequency range (roughly between 10 Hz and 200 Hz), NFR spectra (especially third harmonic  $Y_3$ ) for full cell and the negative electrode are almost identical, i.e., de-/intercalation at the negative electrode dominates, whereas similar as in DRT, contributions from positive electrode come into play at lower frequency range.

In general, similar to impedance, a monotonous relation between PSD and nonlinear responses in the characteristic frequency range of the charge transfer process at the negative electrode can be drawn: The larger the particle size, the smaller the surface area, which is unfavourable to the charge transfer process. Thus, larger impedance and nonlinear response, especially  $Y_3$ , are observed. In none of the cells, significant nonlinearities are observed in the frequency range of  $10^2$  Hz to 1 kHz. This confirms that the processes observed in DRT at this frequency range are no charge-transfer processes but most probably SEI processes and ion transport processes. Interestingly, it seems that the amplitude of the second harmonic,  $Y_2$  and the third harmonic,  $Y_3$ , have different sensitivities to negative and positive electrodes: the positive electrode causes significant  $Y_2$  responses (see F1), whereas the negative electrode causes more  $Y_3$  (see F3). This indicates asymmetry in the charge transfer kinetics, meaning that the energy for de-/intercalation at positive electrode/electrolyte interphase is different, or in other words, the charge transfer coefficient as typically used in the Butler-Volmer equation deviates stronger from 0.5 for the positive electrode.

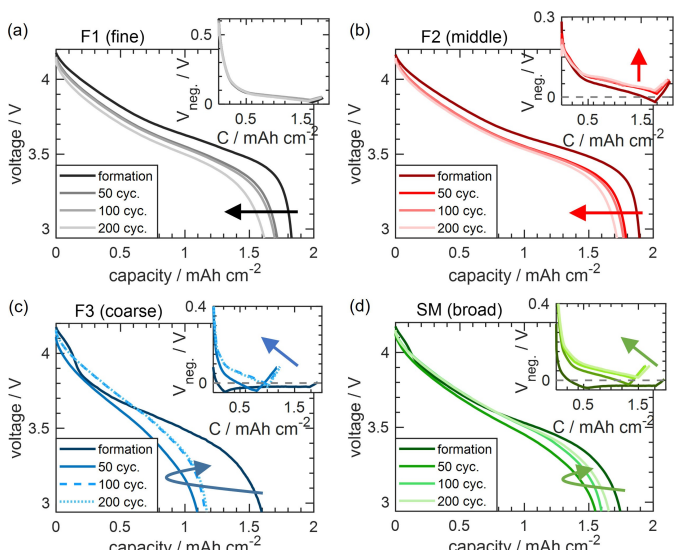
In summary, by combining EIS and NFRA, a clear attribution of frequency response features at certain frequencies to specific processes could be established. F1 (fine) is more dominated by charge transfer at the positive electrode, whereas F3 (coarse) and SM (broad) have very high contributions by charge transfer at the negative electrode.

## Ageing

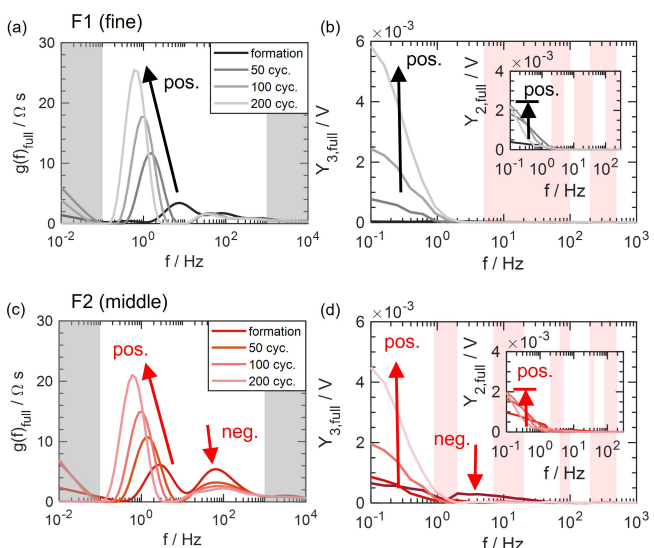
Having established an in-depth understanding of the losses in cells with different active particle sizes of the negative electrode and how they can be monitored with EIS and NFRA, the following section focuses on ageing-induced changes in these cells and their losses.

Figure 3 shows the ageing-related changes in the discharge behaviour and half-cell potential at the negative electrode during cycling for all four PSDs. Thereby, the fine (F1) and medium-sized PSD (F2) have strong similarities to each other, and the coarse (F3) with broad PSD (SM), respectively. Cells with F1 (fine) and F2 (middle) show monotonous capacity fade with cycle number. This is mostly attributable to losses at the positive electrode, as half-cell potential at the negative electrode remains almost constant (see inset). In contrast, cells with F3 (coarse) and SM (broad) show an instantaneous decrease and later increase in capacity. The instantaneous decrease in capacity is attributed to plating at early cycles, which occurs when the potential at the negative electrode drops below zero (see inset). A fraction of the plated lithium reacts irreversibly with electrolyte, forming a new SEI film and leading to a loss in lithium inventory, thus, significant capacity fade. Another possible reason for the capacity fade could be that the micro-cracking leads to the electrical isolation of the active material and is no longer usable for further lithium deintercalation and intercalation. However, as the cells continue to age, the cells recover in capacity. This similar occurrence has also been pointed out in our previous publication.<sup>[14]</sup> One possible reason is the changing of the cycling current (1 C). A significant capacity loss for F3 (coarse) and SM (broad) was observed until the 50<sup>th</sup> cycle, and thus, a current decrease of ca. 3% for SM (broad) and 8% for F3 (coarse) was adapted from the 51<sup>st</sup>, leading to higher capacities (see Supplementary Material S.4). This effect is no longer visible after 100<sup>th</sup> cycle. Therefore, the further capacity increase in SM (broad) might be attributed to the overall kinetic improvement and will be investigated in-depth via EIS and NFRA.

EIS and NFRA allow a deeper look into ageing, and here especially into kinetic changes of the different PSDs. For cells with F1 (fine) and F2 (middle) in Figure 4(a and c), we observe during ageing a significant increase in DRT peak at frequencies



**Figure 3.** Change in 1 C discharge behaviour during cyclic ageing of cells with a) F1 (fine), b) F2 (middle), c) F3 (coarse) and (d) SM (broad) with respective half-cell potential at negative electrode given in insets.



**Figure 4.** Ageing-related changes of cells with F1 (fine) PSD in full cell. a) DRT and b) NFR spectra of  $Y_3$  ( $Y_2$  in inset) and with F2 (middle) PSD in full cell. c) DRT and d) NFR spectra at 25 °C and SOC 50%. Electrode-resolved measurements are given in Figures S.10 and S.11 (DRT), while NFR measurements are in Figures S.12–17 (NFRA).

below 10 Hz, which is attributed mainly to a worsened charge transfer process at the positive electrode. The peak shifts to lower frequencies as the cell ages, further supporting that charge transfer at the positive electrode becomes slower. The ageing-induced increase in the third harmonic  $Y_3$ , Figure 4(b and d), is visible in the same frequency range and thus attributed to worsening charge transfer kinetics of the positive electrode. The increase with worsening charge transfer kinetics is expected, as increased nonlinearity has been shown before for decreased charge transfer kinetic constants, i.e., exchange current densities.<sup>[39,40]</sup> In the frequency range of the negative electrode (>10 Hz), no significant increase in DRT peak or nonlinearities can be seen for cells with F1 (fine). In contrast, negative F2 (middle) electrodes, which already exhibited nonlinear and linear responses for the pristine cells, show a decrease in impedance and nonlinear responses ( $Y_3$ ) during ageing. This suggests a kinetic improvement of the corresponding charge transfer processes at the negative electrode of F2 (middle).<sup>[47]</sup> Contrary to  $Y_3$ , the second harmonics  $Y_2$  provide additional information about the asymmetry behaviour of the charge transfer process.<sup>[39,40,48]</sup> For both F1 (fine) and F2 (middle),  $Y_2$  does not show a monotonous increase. Instead,  $Y_2$  increases mainly at the beginning of cycling up to the 50<sup>th</sup> cycle and only in the frequency range of the positive electrode (see insets of Figure 4 b and d). This implies that the charge transfer process at the positive electrode becomes asymmetric at the beginning of ageing while the kinetics of the charge transfer process at the positive electrode, represented by  $Y_3$  and EIS, continues to deteriorate as the cells age. The change in charge transfer symmetry suggests a qualitative change in the nature of the reaction during ageing. A possible reason may be the migration of transition metals into lithium vacancies in the early cycles, which causes the energy difference in intercalation and

deintercalation as lithium is inserted or removed from different locations.<sup>[49,50]</sup>

For cells with F3 (coarse) and SM (broad) shown in Figures 6 and 7, as they age, the DRT peaks, which are attributed to the charge transfer process as well as ionic transport through SEI at negative electrode decrease and shift to a higher frequency range, which is similar to F2 (middle) and suggests an improvement of the respective kinetics. The kinetic improvement was hypothesized in our prior work<sup>[14]</sup> and also in other publications<sup>[51]</sup> to be caused by the micro-cracking that generates more active surface area and lowers the overpotential for the respective processes. In this study, we prove such microstructural changes and cracks at the negative electrode with scanning electron microscopy for SM (broad) and F3 (coarse) electrodes, as shown in Figure 5.

In addition to our previous work, in which only a small number of cycles were examined, long-term cycling revealed that charge transfer kinetics at the positive electrode, which is presented by the DRT peak in the low-frequency range, interestingly first improves and then worsens as the cell ages. Such a phenomenon has not been observed before and is only visible in longer-term ageing.  $Y_3$  again has a similar trend as impedance, except for the later ageing stage of the cells with F3 (coarse), where only impedance increases at the lower

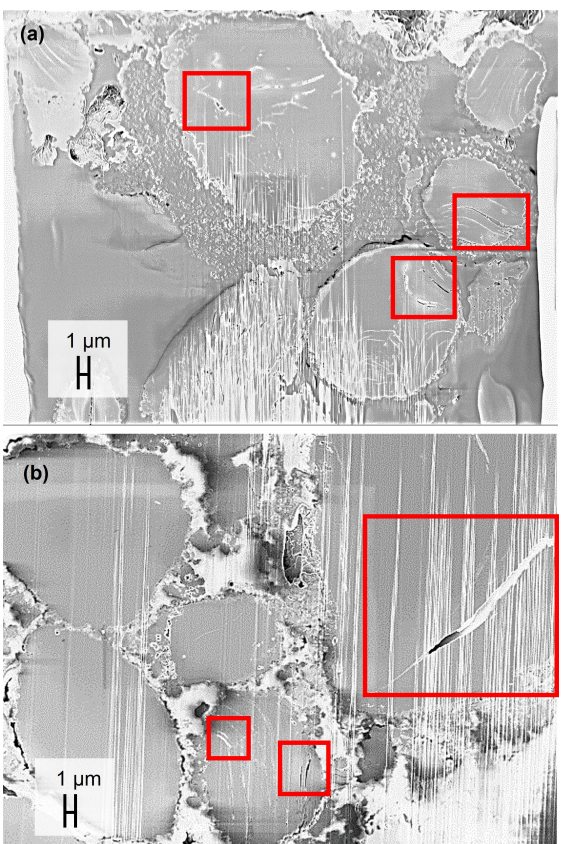


**Figure 5.** Cross-sectional cut by focused ion beam and scanning electron microscope (FIB-SEM) scan of the negative electrode for a) F3 (coarse) and b) SM (broad) show exfoliation and micro-cracking (red-framed region) within the particles. The vertical white stripes are artefacts during sample preparation.

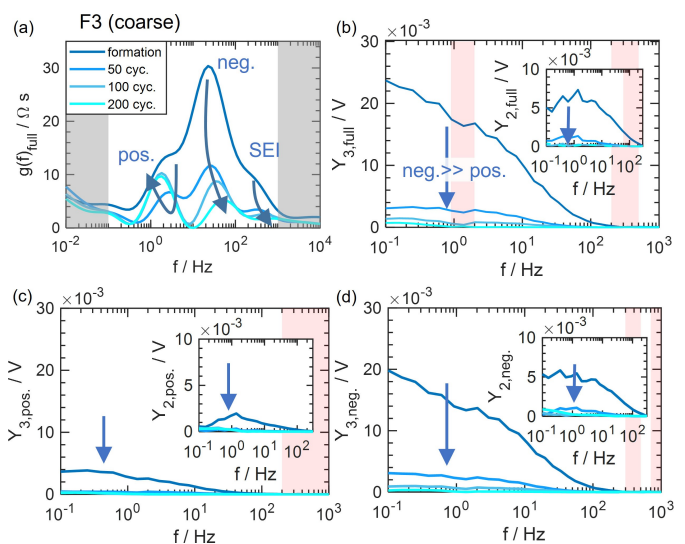


**Figure 6.** Ageing-related changes of cells with F3 (coarse) PSD in full cell. a) DRT and b) NFR spectra of  $Y_3$  ( $Y_2$  in inset) and electrode-resolved NFR spectra at c) negative and d) positive electrodes at 25 °C and SOC 50%.

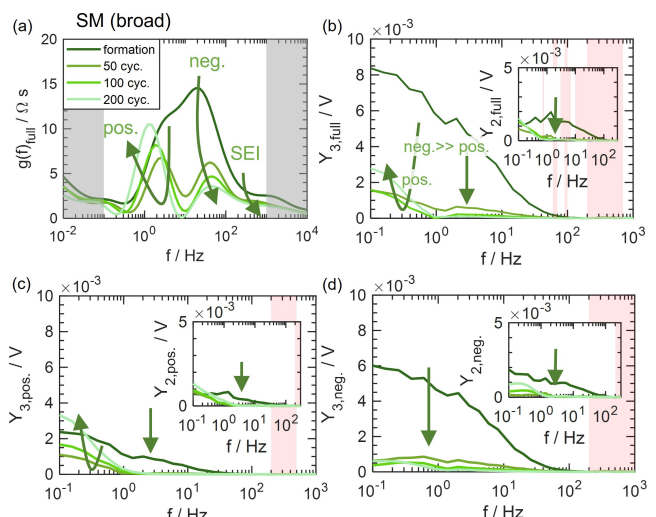


**Figure 7.** Ageing-related changes of cells with SM (broad) PSD in full cell. a) DRT and b) NFR spectra of  $Y_3$  ( $Y_2$  in inset) and electrode-resolved NFR spectra at c) negative and d) positive electrodes at 25 °C and SOC 50%.

frequency. Meanwhile, for cells with SM (broad), a further increase in  $Y_3$  at lower frequencies is visible and identified to be arising from the positive electrode, as shown in Figure 7(d).  $Y_2$  for both cases behaves similarly to  $Y_3$ , whereby it decreases significantly in the frequency range of the negative electrode. This indicates that micro-cracking not only improves the charge transfer kinetics at the negative electrode, represented by EIS and  $Y_3$ , but the charge transfer nature becomes more symmetric. Again, for cells with SM (broad),  $Y_2$  increases after the 100<sup>th</sup> cycle. While comparing the electrode-resolved measurements in Figure 7(c and d), one could notice that the charge transfer process at the positive as well as negative electrodes becomes asymmetric as the cells age.

## Information content of NFRA vs. discharge curves and EIS

Overall, discharge curves, EIS (DRT) and NFRA were shown to give complementary insights into the effect of electrode design and the ageing behaviour of Li-ion batteries. NFRA is a new technique, so we would like to compare the techniques regarding their information content. Discharge curves yield combined kinetic and mass transport losses, which affect the discharge trajectory and the gained capacity. Via discharge curves alone, one cannot deconvolute the losses attributed to the kinetic or transport losses. Frequency response analysis fills this gap. EIS enables the identification of losses by different underlying processes. For example, kinetic losses for the charge transfer process at respective electrodes and the transport loss through SEI can be separately identified. NFRA allows discrimination between charge transfer and transport processes through SEI by their nonlinear behaviour, whereby the transport process through SEI is almost linear and is not visible in NFR spectra. NFRA provides additional information on the symmetry of the charge transfer process via  $Y_2$ , suggesting qualitative surface changes, e.g., due to mechanistic changes. Furthermore, the ageing trend of  $Y_2$  is different from  $Y_3$ , which might give extra information on the nature of ageing nature. Thus, NFRA yields highly valuable information on the nature and degree of ageing.

## Conclusions

The ageing behaviour of lithium-ion batteries with different PSD of negative graphitic electrodes and NMC-111 is assessed in detail using various electrode-resolved measurements. Discharge curves are complemented by EIS and, for the first time, NFRA to separately analyze kinetic and transport processes. NFRA allows additional identification of the nonlinear kinetic contributions. In addition to our prior work, we found out that the PSD of the negative electrode determines whether the negative or positive electrode is showing the highest charge transfer kinetic losses. Strongly different ageing behaviour is observed for cells with different PSD, which are dominated by either negative or positive electrode ageing. On the one hand, for cells with small to middle-sized particles at the negative electrode, we observed before cycling, the charge transfer kinetic loss at the positive electrode is more dominant than the negative electrode. As cycling begins, the positive electrode is, therefore, more stressed and aged, causing a consistent reduction in discharge capacity; specifically, in this work, we identified the increase in EIS and NFRA due to the dominant degradation of charge transfer at the positive electrode. On the other hand, for cells with coarse and broad PSD at the negative electrode, we observed firstly a decrease and then recovery in discharge capacity, EIS and NFRA. This finding is due to the kinetic improvement of the charge transfer process at the negative electrode, resulting from the micro-cracking as suggested in our previous publication and first-time evidenced by the FIB-SEM scan in this study. Meanwhile, the charge transfer process at the positive electrode also shows a slight

increment in EIS as well as NFRA in the later cycling stage for coarse and broad PSDs that was not observed in our prior work due to only a small cycle number, which suggests the degradation of the positive electrode becomes increasingly significant when the cells continue to age in the long term. Via second harmonic  $Y_2$ , we further identified that the positive electrode shows stronger charge transfer asymmetry, whereas the negative electrode is dominated by third harmonic  $Y_3$  due to inferior charge transfer kinetics. Also,  $Y_2$  shows a different ageing trend than impedance and  $Y_3$ , which we believe could be related to the change in charge transfer symmetry during cell ageing.

As an outlook, NFRA has proven to be an essential tool for obtaining additional information on the nature of kinetic and surface-related processes. We consider it highly interesting to correlate NFRA with surface analysis tools, which should give more information on the physical processes causing the change in charge transfer symmetry. NFRA may become a standard tool for easy and early detection of mechanistic surface changes. We also suggest widespread usage of this tool, also for other battery chemistries and analysis tasks. Overall, we have shown for the first time in this study that the strong interplay of the ageing behaviour between both positive and negative electrodes depends on the PSDs of the negative electrode. Thus, for electrode engineering, it is critical to always inspect and optimize both negative and positive electrodes simultaneously.

## Experimental Section

### Electrode production

In this study, we used the negative electrodes published in<sup>[14]</sup> with three fractions of different PSD and the source material. The active material for the negative material was artificial graphite mesocarbon microbeads powder (MCMB) from Osaka Gas Chemicals Co. Ltd, which has an average specific capacity of  $325 \text{ mAh g}^{-1}$ .<sup>[14]</sup> Table 1 shows the characterization results of the negative electrodes. Positive electrodes from Customcells were used in this study. The selected positive electrode has an average specific capacity of  $145 \text{ mAh g}^{-1}$  and contains 86 wt.% of active material (NMC-111) and 14 wt.% of additives and binder. The material of positive and

negative electrodes with different PSD in this study is the same as that reported in our previous work.<sup>[14]</sup>

### Cell assembly and ageing experiment

Electrochemical characterization was done in a commercial three-electrode setup (PAT-Cell) from EL-CELL GmbH. In between positive and negative electrodes, a commercial separator (EL-CELL GmbH, ECC1-00-0210-V/X) of polypropylene (PP) and polyethylene (PE) with a thickness of  $220 \mu\text{m}$  and a built-in lithium reference ring was used. As the electrolyte,  $103 \mu\text{L}$  mixtures of ethylene carbonate (EC) and dimethyl carbonate (DMC) with a ratio of 1:1 (v/v) and  $1 \text{ M}$  lithium hexafluorophosphate ( $\text{LiPF}_6$ ) were used. The whole cell assembly process was completed inside an argon-filled glovebox ( $\text{O}_2$  and  $\text{H}_2\text{O} < 0.1 \text{ ppm}$ ). For reproducibility, three cells were built for each fraction of a given PSD. The freshly built cells were first rested for 12 hours in a temperature chamber (ESPEC EUROPE GmbH, SU 642) at  $25^\circ\text{C}$ . After that, the cells were subjected to formation and cycled using a battery cycler (MACCOP INC., Series 4000). During the formation step, the cells were charged and discharged with C/10 in the constant current (CC) step for two cycles and constant current-constant voltage (CC-CV) step for one cycle between  $2.9 \text{ V}$  and  $4.2 \text{ V}$  at  $25^\circ\text{C}$ . The CV step was stopped when the charging current was reduced to C/20. Within a similar voltage window and temperature, the ageing experiment was conducted at 1 C in CC-CV step. The abort criterion for the ageing experiment was when either of the cells had reached the State of Health (SOH) 60% (60% of its initial capacity) or 200 cycles. The protocols for the formation cycle and the ageing experiment are detailed in Table 2.

### Electrochemical characterization

EIS and NFRA were conducted at  $25^\circ\text{C}$  and SOC 50% right after the formation step at the 4<sup>th</sup> cycle, after the 50<sup>th</sup> cycle and after every consecutive 100 cycles using Zahner Zennium electrochemical workstation. SOC 50% was adjusted by discharging the cell from a fully charged state at  $4.2 \text{ V}$  by C/10 for 5 hours, whereby the SOC-adjustment current depended on the capacity that was measured from the previous characterization series. For example, the SOC-adjustment current for the characterization at the 100<sup>th</sup> cycle is determined from the capacity that was characterized at the 50<sup>th</sup> cycle. For EIS, the cells were measured under galvanostatic mode with an excitation amplitude of  $500 \mu\text{A}$  and a frequency range between  $10 \text{ mHz}$  and  $10 \text{ kHz}$ . As for NFRA, the cells were measured under a similar measurement mode but at a higher excitation amplitude of  $10 \text{ mA}$  and a smaller frequency range between  $100 \text{ mHz}$  and  $1 \text{ kHz}$ . The amplitudes of up to nine harmonics  $Y_{2,3}$  were measured, which correspond to multiples of the fundamental frequency  $f_1$ . During NFR measurement, the cells were moderately excited, giving rise to only the second harmonic  $Y_2$  and third harmonic  $Y_3$  with sufficient signal-to-noise ratio so that the interaction between the higher harmonics can be minimized.<sup>[36]</sup>

**Table 1.** Characteristic of the different particle fractions and their corresponding source material from negative electrode.<sup>[14]</sup>

Material	Acronym	$X_{50}^{[a]}$ [ $\mu\text{m}$ ]	$\epsilon_{\text{C,ML}}^{[b]}$ [%]	$d^{[c]}$ [ $\mu\text{m}$ ]	$S_v^{[d]}$ [ $\text{m}^2 \text{ cm}^{-3}$ ]	$C_{\text{theo}}^{[e]}$ [mAh]
Source material	SM (broad)	12.90	50	74	1.36	5.05
Fraction 1	F1 (fine)	1.53	45	78	4.31	4.99
Fraction 2	F2 (middle)	5.86	45	69	1.06	5.19
Fraction 3	F3 (coarse)	17.45	59	66	0.38	5.15

[a] median particle size. [b] porosity based on the coating mass loading on the electrode, the resulting mass loading for all negative electrodes was  $8.9 \text{ mg cm}^{-2}$ . [c] electrode thickness. [d] volumetric specific surface area. [e] theoretical electrode capacity calculated based on the positive electrode.

**Table 2.** Protocol for the formation and ageing experiment.

	Formation	Ageing experiment
Temperature:		$25^\circ\text{C}$
No. of cycles:	3 cycles	200 cycles
Dis-/charging pattern:	CC: CC-CV: Abort criterion for CV:	2 cycles 3 <sup>rd</sup> cycle $I > C/20$ CC: Charge Discharge

## Measurement reliability and data treatment

We are aware that the utilization of a reference ring electrode may lead to artefacts during frequency response measurements, for example, inductive loops in certain frequency ranges of AC impedance<sup>[52,53]</sup> or NFR spectra. Still, it is a useful in-operando analysis technique to obtain the DC potentials and overpotentials of negative and positive electrodes. Symmetrical cells were not applied as the measurements had to be performed during the ageing procedure in a working full cell.<sup>[53]</sup> We identified the frequency range in EIS, where the artefact appears and disregarded the DRT analysis in the artefact range by greying out the specific frequency region in the spectra.

In addition, the measured NFR data must be conditioned according to an algorithm developed in-house. The algorithm diminishes artefacts originating from the potentiostat itself: the measured response signals contain not only responses from the battery but also responses of the battery corresponding to the undesired higher harmonics in the input signal. Furthermore, we only consider those NFRA data as reliable where nonlinear response signals (normalized against the linear signals) are at least 1% of the linear response signals. The unreliable NFRA region is marked in red.

The derivation of DRT from EIS spectra was performed using the in-house established software tool "All-Fit" in MATLAB. For the DRT computation, the regularization parameter  $\lambda$  has shown to be a significant input parameter that could affect the accuracy of DRT analysis: large  $\lambda$  leads to poor deconvoluted DRT peaks (underfitting), while small  $\lambda$  causes erroneous splitting of DRT peaks (overfitting). For more information, please refer to Supporting Information S.1. In this work, an intermediate value of  $\lambda = 10^{-3}$  was selected for the DRT computation.

## Acknowledgements

This project (17IND10 – LiBforSecUse) has received funding from the EMPIR program, co-financed by the Participating States and from the European Union's Horizon 2020 research and innovation program. Dr.-Ing. Jochen Joos and Annette Schucker supported FIB-SEM analysis. Julian Ulrich supported the conditioning of NFR data.. Open Access funding enabled and organized by Projekt DEAL.

## Conflict of Interests

These authors declare no conflict of interest.

## Data Availability Statement

The data that support the findings of this study are available from the corresponding author upon reasonable request.

**Keywords:** polydispersity · electrode-resolved analysis · electrochemical impedance spectroscopy · distribution of relaxation time · nonlinear frequency response analysis · electrochemistry · surface analysis

- [1] M. J. Lain, J. Brandon, E. Kendrick, *Batteries* **2019**, *5*, 64–75.
- [2] D.-W. Chung, P. R. Shearing, N. P. Brandon, S. J. Harris, R. E. García, *J. Electrochim. Soc.* **2014**, *161*, A422–A430.
- [3] R. Darling, J. Newman, *J. Electrochim. Soc.* **1997**, *144*, 4201–4208.
- [4] S. T. Taleghani, B. Marcos, K. Zaghib, G. Lantagne, *J. Electrochim. Soc.* **2017**, *164*, E3179–E3189.
- [5] F. Hasan, J. Kim, H. Song, S. H. Lee, J. H. Sung, J. Kim, H. D. Yoo, *J. Electrochim. Sci. Technol.* **2020**, *11*, 352–360.
- [6] M. Jo, Y.-S. Hong, J. Choo, J. Cho, *J. Electrochim. Soc.* **2009**, *156*, A430–A434.
- [7] S. P. Sheu, C. Y. Yao, J. M. Chen, Y. C. Chiou, *J. Power Sources* **1997**, *68*, 533–535.
- [8] Y. Liu, H. Liu, X. Zhao, L. Wang, G. Liang, *Journal of Wuhan University of Technology-Mater. Sci. Ed.* **2019**, *34*, 549–557.
- [9] H. Liu, J. Wang, X. Zhang, D. Zhou, X. Qi, B. Qiu, J. Fang, R. Kloepsch, G. Schumacher, Z. Liu, J. Li, *ACS Appl. Mater. Interfaces* **2016**, *8*, 4661–4675.
- [10] L. Kun, K. Dongsuk, in *2016 IEEE Transportation Electrification Conference and Expo, Asia-Pacific (ITEC Asia-Pacific)*, **2016**, pp. 454–459.
- [11] M. Meyer, L. Komisyska, B. Lenz, C. Agert, *Appl. Immunohistochem.* **2013**, *37*, 2016–2027.
- [12] I. Hwang, C. W. Lee, J. C. Kim, S. Yoon, *Mater. Res. Bull.* **2012**, *47*, 73–78.
- [13] D. Beck, P. Dechent, M. Junker, D. U. Sauer, M. Dubarry, *Energies*, Vol. *14*, **2021**.
- [14] L. Bläubaum, F. Röder, C. Nowak, H. S. Chan, A. Kwade, U. Kremer, *ChemElectroChem* **2020**, *7*, 4755–4766.
- [15] H. Buqa, D. Goers, M. Holzapfel, M. E. Spahr, P. Novák, *J. Electrochim. Soc.* **2005**, *152*, A474–A481.
- [16] F. Röder, S. Sonntag, D. Schröder, U. Kremer, *Energy Technol.* **2016**, *4*, 1588–1597.
- [17] C. Gan, C. Zhang, W. Wen, Y. Liu, J. Chen, Q. Xie, X. Luo, *ACS Appl. Mater. Interfaces* **2019**, *11*, 35809–35819.
- [18] T. Huang, Y. Yang, K. Pu, J. Zhang, M. Gao, H. Pan, Y. Liu, *RSC Adv.* **2017**, *7*, 2273–2280.
- [19] W.-R. Liu, Z.-Z. Guo, W.-S. Young, D.-T. Shieh, H.-C. Wu, M.-H. Yang, N.-L. Wu, *J. Power Sources* **2005**, *140*, 139–144.
- [20] S. E. Lee, J. H. Kim, Y.-S. Lee, B. C. Bai, J. S. Im, *Carbon Lett.* **2021**, *31*, 911–920.
- [21] Y. Sato, T. Nakano, K. Kobayakawa, T. Kawai, A. Yokoyama, *J. Power Sources* **1998**, *75*, 271–277.
- [22] E. Pohjalainen, T. Rauhala, M. Valkeapää, J. Kallioinen, T. Kallio, *J. Phys. Chem. C* **2015**, *119*, 2277–2283.
- [23] A. K. Rai, L. T. Anh, J. Gim, V. Mathew, J. Kang, B. J. Paul, J. Song, J. Kim, *Electrochim. Acta* **2013**, *90*, 112–118.
- [24] I. Capone, K. Hurlbutt, A. J. Naylor, A. W. Xiao, M. Pasta, *Energy Fuels* **2019**, *33*, 4651–4658.
- [25] M. Klett, R. Eriksson, J. Groot, P. Svens, K. Ciosek Höglström, R. W. Lindström, H. Berg, T. Gustafson, G. Lindbergh, K. Edström, *J. Power Sources* **2014**, *257*, 126–137.
- [26] M. Winter, P. Novák, A. Monnier, *J. Electrochim. Soc.* **1998**, *145*, 428.
- [27] D. Goers, M. E. Spahr, A. Leone, W. Märkle, P. Novák, *Electrochim. Acta* **2011**, *56*, 3799–3808.
- [28] M. E. Spahr, D. Goers, W. Märkle, J. Dentzer, A. Würsig, H. Buqa, C. Vix-Guterl, P. Novák, *Electrochim. Acta* **2010**, *55*, 8928–8937.
- [29] M. Weiss, R. Ruesj, J. Kasnatscheew, Y. Levartovsky, N. R. Levy, P. Minnmann, L. Stolz, T. Waldmann, M. Wohlfahrt-Mehrens, D. Aurbach, M. Winter, Y. Ein-Eli, J. Janek, *Adv. Energy Mater.* **2021**, *11*, 2101126.
- [30] T. G. Zavalis, M. Klett, M. H. Kjell, M. Behm, R. W. Lindström, G. Lindbergh, *Electrochim. Acta* **2013**, *110*, 335–348.
- [31] S. S. Zhang, L. Ma, J. L. Allen, J. A. Read, *J. Electrochim. Soc.* **2021**, *168*, 040519.
- [32] R. Xiong, Y. Yu, S. Chen, M. Li, L. Li, M. Zhou, W. Zhang, Y. Bo, D. Li, H. Yang, Y. Zhang, H. Zhou, *J. Power Sources* **2023**, *553*, 232296.
- [33] A. Lasia, in *Mod. Aspects Electrochem.* (Eds.: B. E. Conway, J. O. M. Bockris, R. E. White), Springer US, Boston, MA, **2002**, pp. 143–248.
- [34] D. D. Macdonald, *Electrochim. Acta* **2006**, *51*, 1376–1388.
- [35] P. Su-Moon, Y. Jung-Suk, *Anal. Chem.* **2003**, *75*, 455A–461A.
- [36] N. Harting, N. Wolff, F. Röder, U. Kremer, *Electrochim. Acta* **2017**, *248*, 133–139.
- [37] N. Wolff, N. Harting, M. Heinrich, U. Kremer, *Electrochim. Acta* **2019**, *298*, 788–798.
- [38] N. Wolff, N. Harting, M. Heinrich, F. Röder, U. Kremer, *Electrochim. Acta* **2018**, *260*, 614–622.
- [39] M. D. Murbach, D. T. Schwartz, *J. Electrochim. Soc.* **2017**, *164*, E3311–E3320.

- [40] N. Wolff, N. Harting, F. Röder, M. Heinrich, U. Krewer, *European Phys. J. Special Topics* **2019**, 227, 2617–2640.
- [41] N. Harting, N. Wolff, U. Krewer, *Electrochim. Acta* **2018**, 281, 378–385.
- [42] N. Harting, R. Schenkendorf, N. Wolff, U. Krewer, *Appl. Sci.* **2018**, 8, 821–835.
- [43] N. Harting, N. Wolff, F. Röder, U. Krewer, *J. Electrochem. Soc.* **2019**, 166, A277–A285.
- [44] T. H. Wan, M. Saccoccia, C. Chen, F. Ciucci, *Electrochim. Acta* **2015**, 184, 483–499.
- [45] J. Illig, M. Ender, A. Weber, E. Ivers-Tiffée, *J. Power Sources* **2015**, 282, 335–347.
- [46] J. Costard, J. Joos, A. Schmidt, E. Ivers-Tiffée, *Energy Technol.* **2021**, 9, 2000866.
- [47] D. Witt, F. Röder, U. Krewer, *Batteries & Supercaps* **2022**, 5, e202200067.
- [48] M. D. Murbach, V. W. Hu, D. T. Schwartz, *J. Electrochem. Soc.* **2018**, 165, A2758–A2765.
- [49] R. A. House, G. J. Rees, M. A. Pérez-Osorio, J.-J. Marie, E. Boivin, A. W. Robertson, A. Nag, M. Garcia-Fernandez, K.-J. Zhou, P. G. Bruce, *Nat. Energy* **2020**, 5, 777–785.
- [50] A. Van der Ven, K. A. See, L. Pilon, *Battery Energy* **2022**, 1, 20210017.
- [51] P. Shafiei Sabet, A. J. Warnecke, F. Meier, H. Witzenhausen, E. Martinez-Laserna, D. U. Sauer, *J. Power Sources* **2020**, 449, 227369.
- [52] M. Ender, J. Illig, E. Ivers-Tiffée, *J. Electrochem. Soc.* **2017**, 164, A71–A79.
- [53] J. P. Schmidt, T. Chrobak, M. Ender, J. Illig, D. Klotz, E. Ivers-Tiffée, *J. Power Sources* **2011**, 196, 5342–5348.

---

Manuscript received: May 12, 2023

Revised manuscript received: July 8, 2023

Accepted manuscript online: July 12, 2023

Version of record online: July 27, 2023

---